Imaging Tumor-Infiltrating Lymphocytes in Brain Tumors with [^{64}Cu]Cu-NOTA-anti-CD8 PET

Veronica L. Nagle[1], Kelly E. Henry[2], Charli Ann J. Hertz[3], Maya S. Graham[4,5], Carl Campos[3], Luis F. Parada[4,6], Neeta Pandit-Taskar[2,7,8], Andrea Schietinger[9], Ingo K. Mellinghoff[1,3,4,5], and Jason S. Lewis[1,2,7,10,11]

ABSTRACT

Purpose: Glioblastoma (GBM) is the most common malignant brain tumor in adults. Various immunotherapeutic approaches to improve patient survival are being developed, but the molecular mechanisms of immunotherapy resistance are currently unknown. Here, we explored the ability of a humanized radiolabeled CD8-targeted minibody to noninvasively quantify tumor-infiltrating CD8-positive (CD8$^+$) T cells using PET.

Experimental Design: We generated a peripheral blood mononuclear cell (PBMC) humanized immune system (HIS) mouse model and quantified the absolute number of CD8$^+$ T cells by flow cytometry relative to the [^{64}Cu]Cu-NOTA-anti-CD8 PET signal. To evaluate a patient-derived orthotopic GBM HIS model, we intracranially injected cells into NOG mice, humanized cohorts with multiple HLA-matched PBMC donors, and quantified CD8$^+$ tumor-infiltrating lymphocytes by IHC. To determine whether [^{64}Cu]Cu-NOTA-anti-CD8 images brain parenchymal T-cell infiltrate in GBM tumors, we performed PET and autoradiography and subsequently stained serial sections of brain tumor tissue by IHC for CD8$^+$ T cells.

Results: Nontumor-bearing NOG mice injected with human PBMCs showed prominent [^{64}Cu]Cu-NOTA-anti-CD8 uptake in the spleen and minimal radiotracer localization to the normal brain. NOG mice harboring intracranial human GBMs yielded high-resolution PET images of tumor-infiltrating CD8$^+$ T cells. Radiotracer retention correlated with CD8$^+$ T-cell numbers in spleen and tumor tissue. Our study demonstrates the ability of [^{64}Cu]Cu-NOTA-anti-CD8 PET to quantify peripheral and tumor-infiltrating CD8$^+$ T cells in brain tumors.

Conclusions: Human CD8$^+$ T cells infiltrate an orthotopic GBM in a donor-dependent manner. Furthermore, [^{64}Cu]Cu-NOTA-anti-CD8 quantitatively images both peripheral and brain parenchymal human CD8$^+$ T cells.

Introduction

The treatment of human cancer has been transformed by the observation of long-lasting tumor responses to antibodies blocking the cytotoxic T lymphocyte–associated protein 4 (CTLA-4) or the programmed cell death 1 (PD-1) pathway. Durable clinical responses of otherwise treatment-refractory cancers have also been observed following the infusion of autologous T cells engineered to express a chimeric antigen receptor (CAR). Unfortunately, however, adoptive T-cell transfer and the release of negative regulators of immune activation (immune checkpoints) are currently only effective against certain types of cancer and there remains an urgent need to define how immune responses can be further manipulated to enhance anticancer immunity (1).

The limitations of cancer immunotherapy are particularly apparent in glioblastoma (GBM), the most common malignant primary brain tumor in adults. While immune responses can be elicited to antigens that are expressed in the central nervous system (2, 3), attempts to treat GBM with antibodies blocking the PD-1 pathway or other immune-directed therapies have failed to improve patient survival (4). Treatment resistance in GBM has been attributed to a variety of factors, including systemic immunosuppression, an immunosuppressive tumor microenvironment (TME), and tumor-induced sequestration of T cells in bone marrow (5, 6).

Tumor-infiltrating lymphocytes (TILs), in particular CD8-positive (CD8$^+$) T cells, play a central role in antitumor immunity; their presence within the TME has been associated with improved responses to cancer immunotherapy (7). Noninvasive *in vivo* quantification of CD8$^+$ T cells using radiolabeled fragments of anti-CD8 antibodies represents an attractive approach to guide the clinical development of novel cancer immunotherapies and monitor treatment responses. In prior studies, radiolabeled anti-CD8 minibodies (8) and anti-CD8-cys diabodies (9) have retained their antigen specificity, did not deplete CD8$^+$ T cells, and showed specific uptake in the spleen and lymph nodes of mice by PET. A ^{89}Zr-labeled humanized anti-CD8 minibody showed favorable biodistribution to CD8$^+$ T-cell–rich human tissues in an early-phase clinical trial (10). While this prior study illustrates the safety profile and potential utility of the tracer, questions still remain regarding its quantitative capacity and potential utility for brain tumor imaging. As the number of CD8$^+$ T cells both in the TME and the

[1]Department of Pharmacology, Weill Cornell Medical College, New York, New York. [2]Department of Radiology, Memorial Sloan Kettering Cancer Center, New York, New York. [3]Human Oncology and Pathogenesis Program, Memorial Sloan Kettering Cancer Center, New York, New York. [4]Brain Tumor Center, Memorial Sloan Kettering Cancer Center, New York, New York. [5]Department of Neurology, Memorial Sloan Kettering Cancer Center, New York, New York. [6]Cancer Biology and Genetics Program, Memorial Sloan Kettering Cancer Center, New York, New York. [7]Department of Radiology, Weill Cornell Medical College, New York, New York. [8]Parker Institute for Cancer Immunotherapy, Memorial Sloan Kettering Cancer Center, New York, New York. [9]Immunology Program, Memorial Sloan Kettering Cancer Center, New York, New York. [10]Molecular Pharmacology Program, Memorial Sloan Kettering Cancer Center, New York, New York. [11]Radiochemistry and Molecular Imaging Probes Core, Memorial Sloan Kettering Cancer Center, New York, New York.

Note: Supplementary data for this article are available at Clinical Cancer Research Online (http://clincancerres.aacrjournals.org/).

Corresponding Authors: Jason S. Lewis, Department of Radiology, Memorial Sloan Kettering Cancer Center, 1275 York Avenue, New York, NY 10065. Phone: 646-888-3038; Fax: 646-888-3059; E-mail: lewisj2@mskcc.org; and Ingo K. Mellinghoff, Phone: 646-888-2766; Fax: 646-422-0856; E-mail: mellingi@mskcc.org

Clin Cancer Res 2021;27:1958–66

doi: 10.1158/1078-0432.CCR-20-3243

Translational Relevance

CD8-positive ($CD8^+$) T lymphocytes play a central role in tumor immunity. Clinicians currently rely on biopsy to query the tumor microenvironment of brain tumors. As biopsy is often inaccessible in brain tumors, our understanding of immunotherapeutic resistance could be advanced through methods that noninvasively localize and quantify human $CD8^+$ T cells. We report the visualization and tracking of intratumoral $CD8^+$ T cells in orthotopic glioblastoma (GBM) tumors using [^{64}Cu]Cu-NOTA-anti-CD8 minibody PET. This may allow clinicians to monitor the $CD8^+$ cytotoxic T-cell compartment throughout immunotherapeutic intervention in patients with GBM.

periphery has implications for immunotherapeutic treatment, we examined the ability of the anti-CD8 minibody, IAB22M2C, to noninvasively quantify $CD8^+$ T cells in the GBM TME and the periphery of a humanized GBM mouse model.

Materials and Methods

Radiolabeling and synthesis of [^{64}Cu]Cu-NOTA-anti-CD8

The humanized anti-CD8 minibody (IAB22M2C) was incubated with an 80-fold excess of 2-S-(4-isothiocyanatobenzyl)-1,4,7-triazacyclononane-1,4,7-triacetic acid (p-SCN-Bn-NOTA) in metal-free PBS at pH 8.8 for 4 hours at 4°C. NOTA-anti-CD8 was purified using Zeba Spin Column (Thermo Fischer Scientific, MWCO 10kDa). [^{64}Cu]$CuCl_2$ was obtained from the University of Washington, St. Louis (St. Louis, MO). NOTA-anti-CD8 (0.5 mg, 6.25 nmol) was diluted to a total reaction volume of 300 μL 250 mmol/L NH_4Ac and incubated with 277.5 MBq (7.5 mCi) ^{64}Cu at 42°C for 30 minutes at pH 5.5 and purified using zeba spin column with PBS. Radiochemical purity was assessed using instant thin later chromatography using a 50 mmol/L EDTA (pH 5) eluent.

Immunoreactivity assay

The specific target-binding fraction of [^{64}Cu]Cu-NOTA-anti-CD8 was determined through a solid-phase immunoreactivity assay utilizing magnetic beads functionalized with streptavidin and biotinylated Human CD8α Protein (Sino Biological, catalog no., 10980-H08H-B-10) according to procedures published previously (11).

Animal models

All animal experiments were performed in accordance with the Institutional Animal Care and Use Committee at Memorial Sloan Kettering (MSK) Cancer Center (New York, NY). To generate humanized immune system (HIS) mice, 10^7 HLA-typed peripheral blood mononuclear cells (PBMC) from a single donor (StemCell Technologies) were injected into the tail vein of 5- to 8-week-old female Central Institute for Experimental Animals (CIEA) NOG mice (Taconic, RRID: IMSR_TAC:NOG). Patient-derived xenograft (PDX) 160721-1 and PDX 160615-1 were derived from recurrent World Health Organization grade IV GBMs. To generate GBM PDX–bearing HIS mice, 6- to 8-week-old female CIEA NOG mice were intracranially implanted with 1 μL containing 25×10^4 PDX 160721-1 cells or PDX 160615-1. Patient-derived cell lines and tumor genetic profiling MSK-IMPACT on passages in mice were provided by the MSK Brain Tumor Center. MSK-IMPACT was completed as described previously (12). For mutations and copy-number alterations see Supplementary Table S1. No *Mycoplasma* testing was performed. The patient-derived cell line was maintained through intracranial passages in NOG mice. Tumors were extracted and cells were frozen for subsequent experiments, and all experiments were performed on PDX passages 3–5. Cells were injected 2 mm to the right of bregma and 3 mm inferior to the skull cap into the striatum of the right hemisphere of the brain. Three weeks following tumor implantation, mice were humanized with PBMCs as described above.

Mouse PET/CT imaging

Radiotracer (0.25–0.38 nmol, 7.4–11.1 MBq in sterile PBS, 130–150 μL) was injected by tail vein and 15-minute static PET/CT images were acquired at 1, 4, 12, and 24 hours using a dual microPET/CT Scanner (Inveon, Siemens). PET timepoints with [^{64}Cu]Cu-NOTA-anti-CD8 were adapted from a time course established previously by Tavaré and colleagues (8). MRIs were acquired 1–2 days prior to radiotracer injection for all tumor-bearing mice. Brain PET/CT/MRI coregistration, cropping, and quantification were completed using VivoQuant Software (version 4.0, InviCRO) as described previously (13).

Human PET/CT imaging

The transaxial image of a patient with normal brain tissue injected with the [^{89}Zr]Zr-Df-IAB22M2C tracer was acquired according to methodology described previously with accordance to U.S. Common Rule (10). The protocol was institutional review board approved and all patients provided written informed consent (ClinicalTrials.gov identifier: NCT03107663).

MRI

Mouse brains were imaged on a 9.4-Tesla Biospec Scanner (Bruker Biospin Corp.) with a 114-cm Bruker gradient coil (maximum gradient strength, 530 mT/m). A Bruker ID 4-cm quadrature volume coil was used for RF excitation and detection. During imaging sessions, mice were anesthetized with 1%–2% isoflurane gas in oxygen and were positioned prone in the scanner. First T2-weighted scout images along three orthogonal orientations were acquired. Then T2-weighted mouse brain images along the trans-axial orientation were acquired covering the whole brain with 16 slices using the rapid acquisition with relaxation enhancement (RARE) fast spin-echo sequence with the following acquisition parameters: slice thickness, 0.5 mm; repetition time, 2.5 seconds; echo time, 33 milliseconds; RARE factor, 8; and spatial resolution, 98×78 μm.

Biodistribution studies

Whole vital organs were collected following transcardial perfusion with PBS. Levels of radioactivity for each organ were measured using a PerkinElmer γ-counter. Tracer uptake, which is expressed by percentage of injected dose per gram of body weight (%ID/g), was calculated as the amount of radioactivity divided by the organ mass and the aforementioned decay-corrected injected dose using mass standards of [^{64}Cu]Cu-NOTA-anti-CD8 injectate.

Autoradiography

Following transcardial perfusion with PBS 24 hours postinjection of [^{64}Cu]-NOTA-anti-CD8, organs of interest (brain or lymph nodes) were embedded in optimal cutting temperature (OCT) compound. Lymph nodes were identified and dissected by experts in the Laboratory of Comparative Pathology at MSK (New York, NY). Once frozen, blocks were sectioned until tissue of interest was reached. One slide, with 3×40–μm sections, and three slides, with 3×10–μm

sections, were taken of striatum, hippocampus, and cerebellum, for autoradiography and subsequent hematoxylin and eosin (H&E) or IHC staining. After exposing the slides designated for autoradiography for 10 half-lives, the film was scanned using a Typhoon phosphoimager. FIJI (version 2.0, RRID:SCR_002285) was used to visualize autoradiography images.

Flow cytometry

Following dissection, splenocytes were mechanically dissociated and filtered through a 45-μm sterile filter. Splenocytes were treated with ACK Lysis Buffer (Gibco) to remove red blood cells. Following this, splenocytes were stained with APC-anti-human-CD45 (BD Biosciences, HI30, catalog no., 560973, RRID: AB_10565969), PE-anti-mouse-CD45 (BD Biosciences, 30-F11, catalog no., 553081, RRID: AB_394611), BUV395-anti-human-CD3 (BD Biosciences UCHT1, catalog no., 563548, RRID:AB_2744387), BV-421-anti-human-CD8 (BioLegend, RPA-T8, catalog no., 301035, RRID: AB_10898322), and LIVE/DEAD Fixable Near-IR Dead Cell Stain Kit (Thermo Fisher Scientific, catalog no., L10119). Pooled splenocytes from all groups were used to generate fluorescence minus one and unstained controls. All samples were fixed in 4% paraformaldehyde. Samples were spiked with Precision Count Beads (BioLegend, catalog no., 424902) for quantification. Analysis was performed using FlowJo (version 10.6.1, RRID:SCR_008520). Flow cytometry was performed on the BD LSRFortessa.

IHC

Following microtome sectioning, IHC was performed using 5-μm-thick coronal sections of formalin-fixed, paraffin embedded, tumor-bearing striatal tissue. Sections were stained using the Ventana Benchmark ULTRA IHC automated staining system. T-cell markers were visualized using anti-human-CD8 (Abcam, SP16, ab101500, RRID: AB_10710024, 1:50) and anti-mouse-CD8α (Cell Signaling Technology, D4W2Z, catalog no., 98941, RRID: AB_2756376, 1:200). Expression was imaged and quantified using the HALO Software (version 3.0.311.228, Indica Labs). For OCT-embedded frozen sections, the detection of CD8 expression by IHC was performed at Molecular Cytology Core Facility, SKI, MSK Cancer Center (New York, NY), using Discovery XT Processor (Ventana Medical Systems, Roche-AstraZeneca). Tissue was incubated with rabbit mAb anti-human-CD8 (Roche, SP57, 0.35 μg/mL, catalog no., 790-4460, RRID: AB_2335985) for 4 hours, followed by 32 minutes incubation with biotinylated goat anti-rabbit IgG (Vector Laboratories, catalog no., PK6101, RRID: AB_2336820) in 5.75 μg/mL concentration. Blocker D, Streptavidin-horseradish peroxidase, and DAB Detection Kit (Ventana Medical Systems) were used according to the manufacturer's instructions.

Statistical analysis

GraphPad Prism (version 7; GraphPad Software, RRID: SCR_002798) was used for statistical analyses of the data. Biodistribution data, spleen blocking data, and brain PET data were analyzed by unpaired, two-tailed Student *t* tests and differences at the 95% confidence level. Immunoreactivity assay was analyzed by ordinary one-way ANOVA. Spleen PET and flow cytometry data were analyzed by Pearson correlation coefficient. *P* values of 0.05 or less were considered significant.

Results

Radiolabeling and synthesis of [^{64}Cu]Cu-NOTA-anti-CD8

The anti-human-CD8α minibody, IAB22M2C, consists of two anti-human CD8α scFv fused to the human IgG1 CH3 domain. We conjugated IAB22M2C to a NOTA chelator and radiolabeled NOTA-anti-CD8 with ^{64}Cu. We used ^{64}Cu as radionuclide for PET imaging because its half-life (12.7 hours) is shorter than that of ^{89}Zr (78.4 hours) and better matched to the plasma half-life of the minibody. Furthermore, ^{64}Cu does not accumulate in the bone, an important consideration for small-animal immune imaging.

Matrix-assisted light desorption ionization–time-of-flight mass spectrometry analysis determined an average of 2.5 chelates per minibody. NOTA-anti-CD8 was radiolabeled with ^{64}Cu in 250 mmol/L NH_4Ac at pH 5.5 and purified with >99%

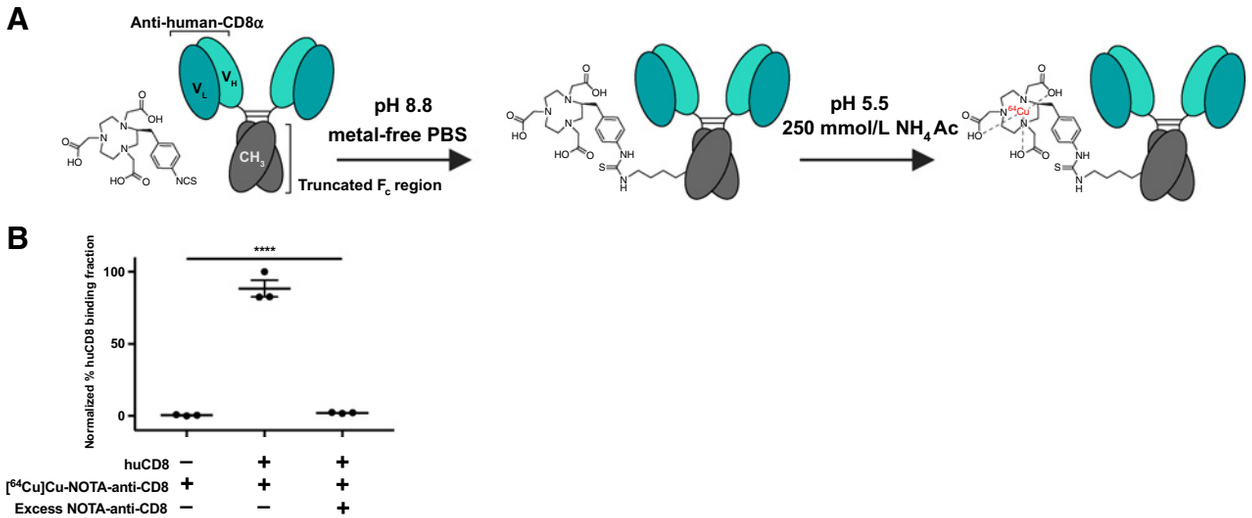

Figure 1.

[^{64}Cu]Cu-NOTA-anti-CD8 reaction scheme and target binding. **A,** [^{64}Cu]Cu-NOTA-anti-CD8 was conjugated to p-SCN-Bn-NOTA chelator and radiolabeled with ^{64}Cu. **B,** Immunoreactivity assay. [^{64}Cu]Cu-NOTA-anti-CD8 bound human CD8 protein *in vitro*, quantified by γ-counting. ****, $P \le 0.0001$. Error bars are the SEM.

radiochemical purity (Supplementary Fig. S1A). [^{64}Cu]Cu-NOTA-anti-CD8–specific activities ranged from 370 to 444 MBq/mg (10–12 mCi/mg) and was stable in human serum at 37°C out to 48 hours (for reaction scheme, see **Fig. 1A**; Supplementary Fig. S1B). Immunoreactivity assay demonstrated [^{64}Cu]Cu-NOTA-anti-CD8 bound human CD8 protein specifically *in vitro* and was blocked to near-control levels by a 100-fold stoichiometric excess of unlabeled NOTA-anti-CD8 ($P < 0.0001$; $f = 223.8$; $df = 8$; one-way ANOVA; **Fig. 1B**).

[^{64}Cu]Cu-NOTA-anti-CD8 targets human T cells in HIS mice

To determine the ability of the humanized anti-CD8 minibody to quantify human CD8$^+$ T cells *in vivo*, we examined the distribution of this radiotracer in immunodeficient mice engrafted with human immune cells, also known as "humanized" mice (14). We used human PBMCs as the source of human immune cells. Severely immunodeficient CIEA NOG mice (referred to as NOG), which carry the SCID mutation and a targeted mutation of the *IL2Rγ* gene on the NOD/ShiJic genetic background, were used as host mice.

We first determined the expansion of human CD8$^+$ T cells in the PBMC HIS model. We injected 10^7 PBMCs into the tail vein of immunocompromised NOG mice ($n = 3$/timepoint; **Fig. 2A**). At weeks 1, 2, and 3 following transfer, spleen cells from HIS (+ PBMCs) and non-HIS (− PBMCs) controls were isolated to determine the proportion of mouse and human CD45$^+$ immune cells of the total number of live cells. The proportion of human CD45$^+$ cells reached 72% ± 13.36% SD at week 3 (**Fig. 2B**, gating strategy; Supplementary Fig. S3). At 3 weeks post–PBMC injection, human CD8$^+$ T cells constituted 59.5% ± 8.71% SD ($n = 3$/group) of all human CD3$^+$ T cells in the mouse spleen (**Fig. 2C**, gating strategy; Supplementary Fig. S3) and NOG mice injected with human PBMCs had significantly larger spleens than mice not injected with human PBMCs (**Fig. 2D** and **E**). These results are consistent with the expected expansion of human CD8$^+$ T cells in the murine spleen following peripheral human PBMC injection in the HIS model (15).

We next determined the ability to image CD8$^+$ T-cell–rich organs using [^{64}Cu]Cu-NOTA-anti-CD8 PET in HIS mice. We first injected human PBMCs and waited 3 weeks to allow for the expansion and distribution of human CD8$^+$ T cells. [^{64}Cu]Cu-NOTA-anti-CD8 was then injected via tail vein into HIS mice (+ PBMCs) or control mice (− PBMCs; $n = 4$/group; **Fig. 2A**). Representative PET/CT images were acquired 4 hours following radiotracer injection (**Fig. 2F**) and showed prominent radiotracer signal in the spleen of PBMC-injected mice. Tracer uptake in lung and liver was also increased, albeit more modestly, in PBMC-injected mice relative to mice without PBMC injection.

To determine PET radiotracer distribution throughout the animals, we extracted relevant tissues at 24 hours postinjection and calculated the %ID/g of tissue by *ex vivo* γ-counting. As expected from the high-resolution immuno-PET images, PBMC-injected HIS mice showed significantly increased uptake of [^{64}Cu]Cu-NOTA-anti-CD8 in the spleens compared with mice without PBMCs (15.6 %ID/g ± 1.2 %ID/g SD vs. 1.2 %ID/g ± 0.4 %ID/g SD; $P < 0.0001$; $t = 21.90$; $df = 6$, two-tailed unpaired *t* test; **Fig. 2G**). The spleens of the PBMC-injected HIS mice harbored dense human CD8$^+$ T-cell infiltrates (**Fig. 2C**). We also observed higher tracer uptake in the liver and lungs of + PBMC (HIS) mice relative to the − PBMC mice (**Fig. 2G**), consistent with the reported redistribution of human CD8$^+$ T cells to the livers and lungs ($P = 0.0005$; $t = 6.273$; $df = 6$ and $P = 0.0001$; $t = 8.636$; $df = 6$, respectively, two-tailed unpaired *t* tests) in the PBMC HIS mouse model. Radiotracer uptake in liver and kidney is likely, at least, in part, related to the metabolism and excretion of the radiotracer through hepatic and renal pathways (ref. 8; **Fig. 2G**).

We sought to determine whether the + PBMC lymph nodes were reconstituted with human CD8$^+$ T cells and whether [^{64}Cu]Cu-NOTA-anti-CD8 localized to lymph nodes in HIS (+ PBMC) mice. At 2 weeks following humanization, we injected + PBMC and − PBMC mice (donor 1, $n = 4$/donor) with [^{64}Cu]Cu-NOTA-anti-CD8 and mice were imaged by PET/CT at 24 hours. Following imaging, we extracted the cervical lymph nodes. The lymph nodes in the − PBMC mice were too small to isolate and thus, autoradiography and IHC on these tissues were unachievable. We performed autoradiography and H&E staining on frozen tissue sections (40 μm) and IHC for human CD8 on the subsequent sections (10 μm) of + PBMC lymph nodes. The H&E staining showed a lack of follicular architecture, which is unusual for lymph nodes. However, the CD8$^+$ infiltrate was repopulating underdeveloped lymph nodes in the immunocompromised NOG background (16), illustrated by the homogenous T-cell distribution in the lymph node seen by IHC. We found that CD8$^+$ T-cell infiltrate corresponded with uptake of the [^{64}Cu]Cu-NOTA-anti-CD8 tracer as visualized by PET and autoradiography (**Fig. 2H**). These results parallel lymph node uptake of ^{89}Zr-Df-IAB22M2C seen in patients with solid malignancies (10).

To determine the quantitative relationship between [^{64}Cu]Cu-NOTA-anti-CD8 uptake and the CD8$^+$ T-cell infiltrate, we measured [^{64}Cu]Cu-NOTA-anti-CD8 uptake by PET and the absolute number of human CD8$^+$ T cells in a CD8$^+$ T-cell–rich organ by flow cytometry. We injected NOG mice with PBMCs from three different PBMC donors (donors 1–3, $n = 3$/donor) to achieve a gradient of human T-cell enrichment. Two and a half weeks following humanization, mice were injected with [^{64}Cu]Cu-NOTA-anti-CD8 and PET/CT images were acquired 24 hours postinjection. Immediately following image acquisition, spleens were harvested, and the absolute number of human CD8$^+$ T cells was counted by flow cytometry. The number of human CD8$^+$ T cells correlated with the %ID/g quantified by PET, demonstrating a quantitative linear relationship between tracer uptake and the absolute number of CD8$^+$ T cells (**Fig. 2I**, $r = 0.8602$; $P < 0.01$, Pearson correlation).

We determined the specificity of [^{64}Cu]Cu-NOTA-anti-CD8 *in vivo*. Two and a half weeks following humanization, HIS (+ PBMC) mice were either injected with [^{64}Cu]Cu-NOTA-anti-CD8 or with [^{64}Cu]Cu-NOTA-anti-CD8 combined with 10-fold stoichiometric excess of unlabeled NOTA-anti-CD8 as a blocking dose ($n = 3$/group). The cold NOTA-anti-CD8 reduced the retention of [^{64}Cu]Cu-NOTA-anti-CD8 by the spleen to radiotracer retention levels of spleens from mice not injected with human PBMCs (**Fig. 2J**, $P = 0.0076$; $t = 4.978$; $df = 4$, two-tailed unpaired *t* test).

The biodistribution of [^{64}Cu]Cu-NOTA-anti-CD8 in the HIS (+ PBMCs) model demonstrated minimal uptake of [^{64}Cu]Cu-NOTA-anti-CD8 in healthy brain, suggesting a suitable signal:noise ratio for use in neuroimaging. To determine whether low baseline brain uptake is also seen in humans, we used PET/CT to image a patient with no brain pathology using the ^{89}Zr-Df-IAB22M2C version of this tracer. At 24 hours, the uptake in normal human brain was low, corresponding to our findings in our HIS mouse model (**Fig. 2K**).

Imaging tumor-infiltrating CD8$^+$ T cells in orthotopic GBM tumors

Given the minimal uptake of the anti-CD8 minibody in normal brain, we explored whether [^{64}Cu]Cu-NOTA-anti-CD8 PET might be able to quantify infiltrating CD8$^+$ T cells in an orthotopic GBM model.

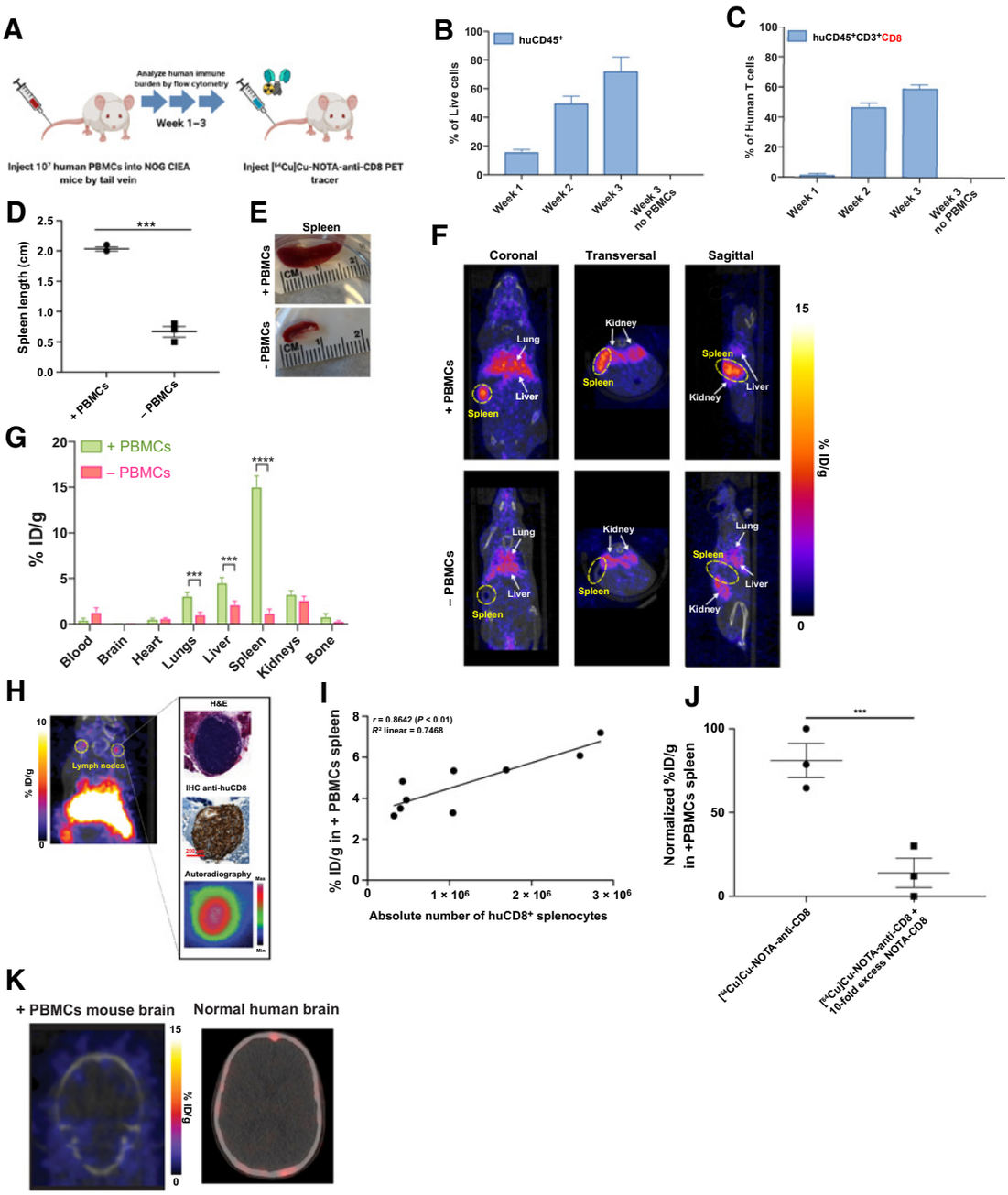

Figure 2.

[^{64}Cu]Cu-NOTA-anti-CD8 targets human CD8$^+$ T cells *in vivo*. **A,** NOG mice were injected with 10^7 human PBMCs and flow cytometry analysis was performed at weeks 1–3 following injection. Mice humanized for 3 weeks were administered [^{64}Cu]Cu-NOTA-anti-CD8 PET tracer. **B** and **C,** Expansion of human CD45$^+$ and human CD8$^+$ immune cells within HIS mice spleens as quantified by flow cytometry. **D,** Spleen length in centimeter 3 weeks following PBMC injection relative to − PBMC control. **E,** Representative images of spleens. **F,** Representative PET/CT images of + PBMC and − PBMC NOG mice 4 hours following [^{64}Cu]Cu-NOTA-anti-CD8 tracer injection ($n = 4$/condition). **G,** *Ex vivo* biodistribution of [^{64}Cu]Cu-NOTA-anti-CD8 24 hours by γ-counting ($n = 4$/condition). **H,** Representative PET/CT scan of HIS mice at 24 hours following [^{64}Cu]Cu-NOTA-anti-CD8 tracer injection ($n = 4$/condition). Yellow dotted circles highlight the cervical lymph nodes. H&E (top, right) and IHC staining (middle, right) for CD8$^+$ T-cell infiltrate and autoradiography (bottom, right) for corresponding [^{64}Cu]Cu-NOTA-anti-CD8 uptake. **I,** Single data points represent an individual HIS mouse 2.5 weeks following PBMC injection. %ID/g was determined by PET. The absolute number of human CD8$^+$ T cells was quantified by whole-spleen flow cytometry following PET imaging. Multiple donors were used to achieve a gradient of absolute T-cell counts ($n = 3$/donor). **J,** Quantification of splenic uptake of [^{64}Cu]Cu-NOTA-anti-CD8 or [^{64}Cu]Cu-NOTA-anti-CD8 plus 10-fold excess cold NOTA-anti-CD8 2.5 weeks following PBMC injection ($n = 3$/condition). **K,** Representative PET/CT imaging of HIS mouse brain 24 hours following [^{64}Cu]Cu-NOTA-anti-CD8 tracer injection ($n = 4$/condition, left). Transaxial coregistered PET/CT image of [^{89}Zr]Zr-Df-IAB22M2C 24 hours post–tracer injection in healthy human brain (right). For all panels ***, $P \le 0.001$; ****, $P \le 0.0001$. Error bars are the SEM.

We intracranially injected NOG mice with GBM cells derived from a human GBM (PDX 160721-1). Three weeks following tumor implantation, mice were humanized with PBMCs partially matched to the HLA of PDX 160721-1 (donor 1). Mouse brains were extracted at week 3 following PBMC injection ($n = 3$/timepoint), and sections were stained by IHC for human and mouse CD8. Human $CD8^+$ T cells infiltrated into the tumor by week 3 following humanization. There was no infiltrate of mouse $CD8^+$ T cells (**Fig. 3A**).

We next determined the ability of [^{64}Cu]Cu-NOTA-anti-CD8 PET to detect $CD8^+$ TILs in orthotopic GBM tumors. Mice without intracranial GBMs (i.e., only receiving intracranial sham injection) and tumor-bearing mice without PBMC injections served as negative controls in these experiments. Mice were imaged at 1, 4, 12, and 24 hours following tracer injection. We observed [^{64}Cu]Cu-NOTA-anti-CD8 accumulation in the tumor site of GBM PDX HIS mice (**Fig. 3B**), but not in controls (Supplementary Fig. S2). This accumulation reflects previous reports indicating minibody-based PET tracer accumulation at the site of interest (17). To determine the region-of-interest and quantify radiotracer uptake by the intracranial tumors, we obtained brain MRI scans 1–2 days prior to PET imaging (**Fig. 3B**, top). The mean uptake of [^{64}Cu]Cu-NOTA-anti-CD8 was 3.7 %ID/g ± 1.2 %ID/g SD, significantly higher than the non-HIS control of 0.5 %ID/g ± 0.1 %ID/g SD within the tumor ($n = 3$–4/group; $P = 0.0027$; $t = 5.227$; $df = 5$, two-tailed unpaired t test; **Fig. 3C**).

We reproduced these findings in a second PDX. We intracranially injected NOG mice with GBM cells derived from second human GBM (PDX 160615-1) and humanized them with PBMCs partially matched to the HLA of PDX 160615-1 (donor 13). + PBMC and − PBMC GBM tumor–bearing mice were imaged at 24 hours following [^{64}Cu]Cu-NOTA-anti-CD8 injection. The mean uptake of [^{64}Cu]Cu-NOTA-anti-CD8 was 1.1 %ID/g ± 0.3 %ID/g SD, again significantly higher than the non-HIS (− PBMCs) control of 0.3 %ID/g ± 0.1 %ID/g SD ($n = 5$/group; $P = 0.0011$; $t = 5.325$; $df = 7$, two-tailed unpaired t test; **Fig. 3D**).

To ensure that [^{64}Cu]Cu-NOTA-anti-CD8 uptake was a result of binding to human $CD8^+$ T cells within the brain parenchyma and not a result of blood pool, both HIS mouse models of GBM were transcardially perfused with PBS following imaging and brains were extracted for autoradiographic analysis. As determined by *ex vivo* autoradiography, [^{64}Cu]Cu-NOTA-anti-CD8 localized to the regions of human $CD8^+$ T-cell infiltrate (IHC), demonstrating the tracer specificity for human $CD8^+$ T cells within the brain parenchyma relative to non-PBMC–infiltrated controls (PDX 160721-1 depicted in **Fig. 3E**; PDX 160615-1 in Supplementary Fig. S4).

GBM is generally considered an immunologically "cold" tumor (6) and yet we observed a high degree of tumor infiltration with $CD8^+$ T cells in PBMC-injected HIS mice. We therefore extended our experiments to PBMCs from multiple other human PBMC donors, either partially (donors 1, and 4–7) or completely (donors 8–12) unmatched to the major HLA loci of the human GBM cells. We observed considerable variability in $CD8^+$ T-cell infiltrations of the intracranial GBMs, with no apparent relationship between the degree of major HLA loci matching ($n = 3$/group; **Fig. 3F**; Supplementary Table S2).

We next repeated our immuno-PET and radiotracer experiments using PBMCs from donors that had resulted in either low, medium, or high level of tumor cell infiltration. Orthotopic GBM PDX tumor–bearing HIS mice were injected with [^{64}Cu]Cu-NOTA-anti-CD8, brains were extracted 24 hours after radiotracer injection, and serial brain sections were cut for autoradiography (40 μm) and IHC (10 μm). The high-resolution autoradiographic signal demonstrated the spatial distribution of [^{64}Cu]Cu-NOTA-anti-CD8 and corresponded with the density of human $CD8^+$ T cells as visualized by IHC (**Fig. 3G**).

We also determined the localization of human $CD8^+$ T cells throughout the brain parenchyma by collecting brain sections (40 μm) throughout the tumor-bearing striatum, as well as nontumor-bearing hippocampus and cerebellum. While there was accumulation of [^{64}Cu]Cu-NOTA-anti-CD8 within the striatum, there was minimal radiotracer signal in tumor-free areas of the brain. We noted a small amount of radiotracer signal in spinal fluid of both PBMC-injected and noninjected mice, representing nonspecific tracer accumulation of the tracer within the cerebrospinal fluid (Supplementary Fig. S5).

We sought to determine whether [^{64}Cu]Cu-NOTA-anti-CD8 uptake quantified by PET corresponded with the density of human $CD8^+$ T cells by IHC across PDXs and donors. To do so, we quantified both the PET signal and T-cell density within each tumor in both PDX 160721-1 and 160615-1 paired with multiple PBMC donors (PDX 160721-1 paired with donors 1 and 2 and PDX 160615-1 paired with donors 13 and 14; $n = 13$). We found that the signal quantified by PET does indeed correlate to the density of human $CD8^+$ T cells within the tumor (**Fig. 2H**; $r = 0.7775$; $P < 0.01$, Pearson correlation). The average tumor uptake in + tumor − PBMC mice was 0.4 %ID/g ± 0.2 %ID/g SD, representing the threshold for nonspecific PET signal in the tumor-bearing brain of this model. The minimum $CD8^+$ T-cell density we were able to quantify by PET beyond this determined threshold was 620 cells/mm^2 (11% of total cells) in this humanized mouse model of GBM.

Discussion

Antibodies blocking the CTLA-4 or PD-1 pathways are effective treatments for brain metastases in patients with melanoma (18) and advanced non–small cell lung cancer (19), but have failed to prolong survival in patients with GBM. Nonetheless, several observations point toward a potential role of immunotherapies for GBM: (i) CAR T therapy has yielded anecdotal clinical responses (20) and increased tumor infiltration by regulatory T cells (21), (ii) short-term PD-1 blockade resulted in increases in TILs in GBM tumor biopsies (22, 23), and (iii) neoantigen-targeting vaccines were able to promote migration of neoantigen-specific T cells from the peripheral blood into intracranial GBM tumors (24). Further progress with immunotherapy for GBM will require the development of novel approaches to evaluate the "cancer immunity cycle" (25), including the trafficking of $CD8^+$ T cells. Our study shows that immuno-PET using a humanized anti-CD8 minibody provides high-resolution images of GBM infiltration by $CD8^+$ T cells in a humanized GBM mouse model and provides a quantitative evaluation of GBM $CD8^+$ TILs and peripheral $CD8^+$ T-cell distribution. The low frequency of radiotracer retention in the normal brain may represent a major advantage over other imaging approaches to quantify immune cell infiltration with PET tracers targeting antigens or metabolic pathways also expressed in healthy brain tissue (26).

Immuno-PET using antibody fragments against mouse $CD8^+$ T cells has been evaluated in nontumor-bearing mice and in mice harboring subcutaneous murine tumors. Both the anti-mouse CD8 minibody (8) and the anti-mouse CD8-cys diabody (9) generated high-resolution PET images of $CD8^+$ T-cell–rich tissues and did not deplete or activate $CD8^+$ T cells. To study the interactions between immune components and GBMs of human origin, we developed a humanized mouse model, consisting of orthotopically implanted human GBM cells and PBMCs from human donors. In tumor-bearing mice,

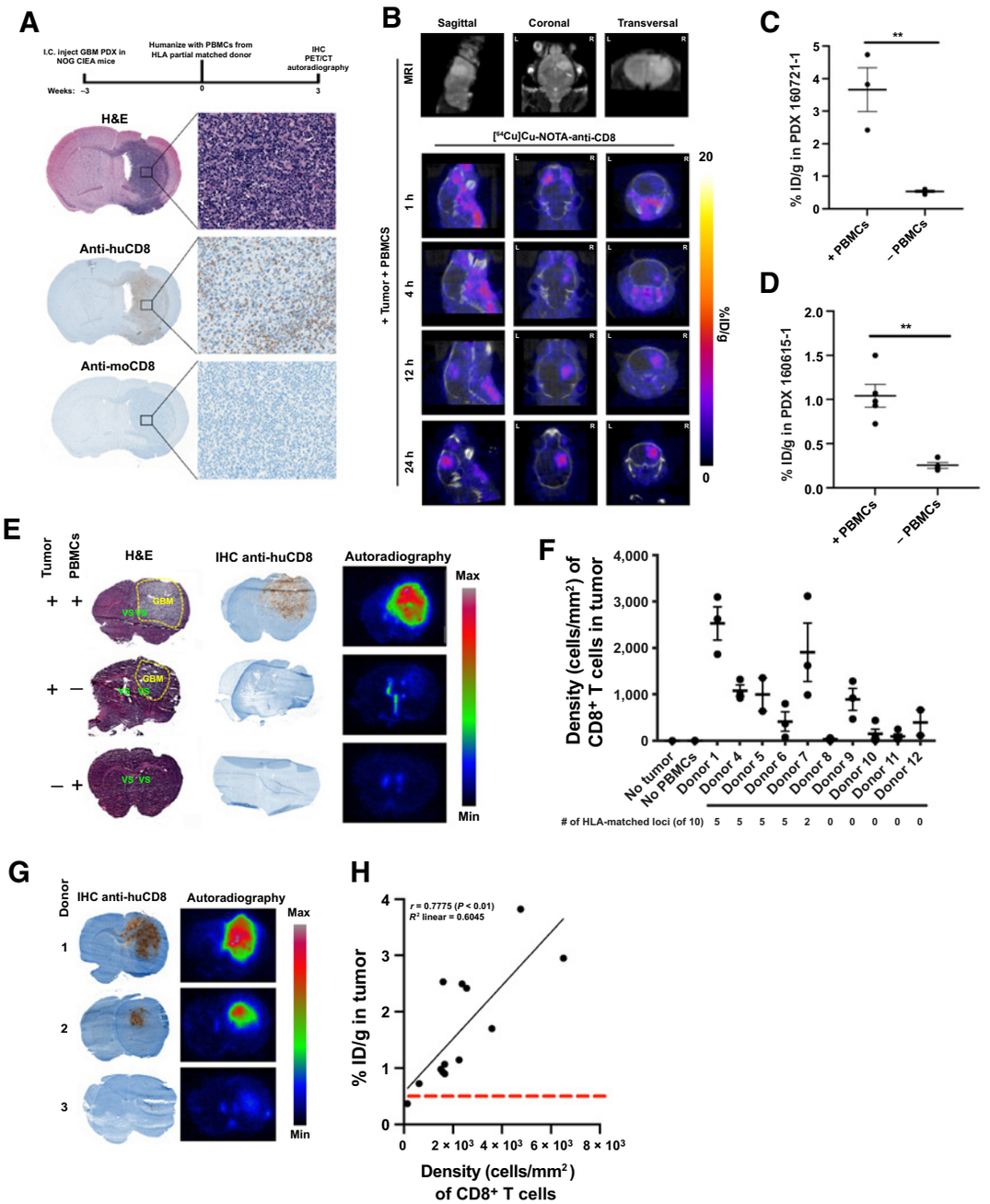

Figure 3.

[^{64}Cu]Cu-NOTA-anti-CD8 images CD8$^+$ human TILs in GBM tumors. **A,** Experimental timeline highlighting the order of PDX engraftment, humanizing, imaging, and necropsy. H&E stains to demarcate GBM PDX 160721-1 at week 3 following humanization (top). IHC staining for human (middle) and mouse (bottom) CD8$^+$ T-cell infiltrate into GBM tumor in serial sections ($n = 3$/timepoint). **B,** MRI 1–2 days prior to [^{64}Cu]Cu-NOTA-anti-CD8 tracer injection (top), coregistered PET/CT images of + PBMCs (donor 1) GBM PDX 160721-1 at 1, 4, 12, and 24 hours following [^{64}Cu]Cu-NOTA-anti-CD8 tracer injection (bottom; $n = 3$/condition). **C,** Quantification of intracranial (I.C.) tumor uptake by PET in GBM PDX 160721-1. Tumor volume region of interest (ROI) determined by MRI. **D,** Quantification of intracranial tumor uptake by PET in GBM PDX 160615-1. Tumor volume ROI determined by MRI. **E,** H&E staining and IHC for human CD8, and autoradiography ($n = 3$/condition) of PDX 160721-1. − Tumor + PBMC mice received a sham intracranial injection. Sections were acquired 24 hours post-radiotracer injection. **F,** Quantification of IHC for human CD8$^+$ T cells in orthotopic GBM PDX 160721-1 across multiple donors ($n = 3$/PBMC donor). No tumor cohort was humanized, but received a sham intracranial injection. No PBMCs bear the PDX, but are not humanized. **G,** IHC for human CD8 and autoradiography in PDX 160721-1 ($n = 3$/condition). Sections were acquired 24 hours post–radiotracer injection. Autoradiography and CD8 IHC were performed on subsequent serial sections. **H,** Quantification of %ID/g in GBM PDXs 160615-1 and 160721-1 relative to CD8$^+$ TIL density. The density of CD8$^+$ T cells was determined by IHC following PET imaging. Each data point represents a single animal. The dotted red line designates the average nonspecific uptake in + tumor − PBMC mice. **, $P \le 0.01$. Error bars are the SEM. VS, ventricular system, includes lateral ventricles, third ventricle, and aquatic space.

radiotracer uptake was closely correlated with human CD8$^+$ T-cell density, determined by IHC staining and autoradiography of adjacent tissue sections. Humanized mice without a brain tumor, on the other hand, showed minimal uptake of the anti-CD8 minibody in the brain despite robust tracer retention in the spleen. Another study recently evaluated the use of ^{89}Zr-labeled desferrioxamine-IAB22M2C (the humanized anti-CD8 minibody) to noninvasively monitor human CD8$^+$ T-cell distribution in CD34$^+$-engrafted humanized mice harboring subcutaneous xenografts of human gastric and cervical cancer cells (27). While our study differs from this prior study in several ways, including the radionuclide (^{64}Cu vs. ^{89}Zr), source of human immune cells (PBMCs vs. CD34$^+$ cells), tumor location (orthotopic vs. subcutaneous), and cancer type, both studies highlight the utility of humanized mice for preclinical immuno-oncology studies (15).

The preclinical evaluation of immunotherapies for GBM has historically relied on syngeneic models, limiting research to a murine tumor immune system (28). Humanized mouse models offer the unique advantage of studying human tumors in a human tumor immune microenvironment in a preclinical setting. However, humanized mouse models have some limitations (15). The PBMC HIS mouse model relies on the transfer of human PBMCs into an immunocompromised mouse. This model primarily reconstitutes human T cells, making it a suitable system to study a human CD8$^+$ T-cell–targeted PET tracer. These mice eventually develop graft-versus-host disease, reducing the experimental window using this model system to 4–6 weeks. To expand the experimental window, NOG mice with the deletion of both MHC class I and class II genes have been used to evaluate effects of immune-targeting agents on subcutaneous human GBM xenografts (29).

Our GBM HIS model is proficient for MHC class I and class II and the PBMC donor was not autologous to the GBM PDX, generating the potential for alloreactivity. Using a single orthotopically implanted human GBM xenograft and PBMCs from 12 different human PBMC donors with different degrees of HLA match, we observed that the degree of tumor infiltration by peripherally injected PBMCs varied considerably between individual PBMC donors. It is plausible that minor HLA mismatches between the tumor and the PBMC donor, rather than differential reactivity to tumor antigens, are primarily responsible for these differences. While the origin of the observed differences in TILs will require further study, these donor-related differences provided a gradient of T-cell densities to document a quantitative relationship between brain parenchymal T-cell infiltrate and [^{64}Cu]Cu-NOTA-anti-CD8 radiotracer retention.

In conclusion, our study demonstrates the ability of [^{64}Cu]Cu-NOTA-anti-CD8 PET to quantify peripheral and tumor-infiltrating CD8$^+$ T cells in brain tumors, which could emerge as an important tool to noninvasively track T-cell responses and immune responses in patients with GBM and other tumors.

Authors' Disclosures

V.L. Nagle reports grants from NIH T32 GM73546 during the conduct of the study. N. Pandit-Taskar reports personal fees and nonfinancial support from ImaginAb during the conduct of the study. I.K. Mellinghoff reports grants from NIH, National Brain Tumor Society, Emerson Collective Cancer Fund, Amgen, General Electric, Lilly, and Kazia, as well as nonfinancial support from ImaginAb Inc, Voyager Therapeutics, and AstraZeneca during the conduct of the study; Dr. Mellinghoff also reports personal fees and other from Roche outside the submitted work. J.S. Lewis reports grants from the Emerson Collective Cancer Fund and the NIH, and reports the supply of reagents from ImaginAb during the conduct of the study. No disclosures were reported by the other authors.

Authors' Contributions

V.L. Nagle: Conceptualization, resources, data curation, software, formal analysis, validation, investigation, visualization, methodology, writing–original draft, project administration, writing–review and editing. **K.E. Henry:** Data curation, formal analysis, validation, investigation, writing–review and editing. **C.A.J. Hertz:** Data curation, formal analysis, investigation, visualization, writing–review and editing. **M.S. Graham:** Data curation, investigation, writing–review and editing. **C. Campos:** Data curation, investigation. **L.F. Parada:** Resources, validation, writing–review and editing. **N. Pandit-Taskar:** Resources, data curation, validation, investigation, writing–review and editing. **A. Schietinger:** Resources, investigation, writing–review and editing. **I.K. Mellinghoff:** Conceptualization, resources, data curation, formal analysis, supervision, validation, investigation, project administration, writing–review and editing. **J.S. Lewis:** Conceptualization, resources, data curation, supervision, validation, investigation, project administration, writing–review and editing.

Acknowledgments

The anti-CD8 minibody (IAB22M2C) was a generous gift from ImaginAb, Inc. We gratefully acknowledge the Molecular Cytology, Flow Cytometry, Comparative Pathology, Radiochemistry and Molecular Imaging Probes, and the Small Animal Imaging Cores at MSK, which are supported by NIH grant P30 CA08748. Flow cytometry analysis was completed with assistance from Kathleen Daniels at the Flow Cytometry Core. Lymph node extraction and histopathology analysis were performed by Jacqueline Candelier, Mark Devaughn, and Adam Michel of the Comparative Pathology Core. This study was supported by NIH NINDS R35 NS105109-01 (to I.K. Mellinghoff), NCI R35 CA232130 (to J.S. Lewis), NIH T32 GM73546 (to V.L. Nagle), the National Brain Tumor Society Defeat GBM initiative (to I.K. Mellinghoff), and the Emerson Collective Cancer Fund (to I.K. Mellinghoff, J.S. Lewis, and A. Schietinger). **Figure 2A** was made in Biorender.com.

The costs of publication of this article were defrayed in part by the payment of page charges. This article must therefore be hereby marked *advertisement* in accordance with 18 U.S.C. Section 1734 solely to indicate this fact.

Received August 17, 2020; revised December 15, 2020; accepted January 15, 2021; published first January 25, 2021.

References

1. Chen DS, Mellman I. Elements of cancer immunity and the cancer-immune set point. Nature 2017;541:321–30.
2. Louveau A, Herz J, Alme MN, Salvador AF, Dong MQ, Viar KE, et al. CNS lymphatic drainage and neuroinflammation are regulated by meningeal lymphatic vasculature. Nat Neurosci 2018;21:1380–91.
3. Song E, Mao T, Dong H, Boisserand LSB, Antila S, Bosenberg M, et al. VEGF-C-driven lymphatic drainage enables immunosurveillance of brain tumours. Nature 2020;577:689–94.
4. Wen PY, Weller M, Lee EQ, Alexander BA, Barnholtz-Sloan JS, Barthel FP, et al. Glioblastoma in adults: a Society for Neuro-Oncology (SNO) and European Society of Neuro-Oncology (EANO) consensus review on current management and future directions. Neuro Oncol 2020;22:1073–113.
5. Chongsathidkiet P, Jackson C, Koyama S, Loebel F, Cui X, Farber SH, et al. Sequestration of T cells in bone marrow in the setting of glioblastoma and other intracranial tumors. Nat Med 2018;24:1459–68.
6. Platten M, Reardon DA. Concepts for immunotherapies in gliomas. Semin Neurol 2018;38:62–72.
7. Gooden MJ, de Bock GH, Leffers N, Daemen T, Nijman HW. The prognostic influence of tumour-infiltrating lymphocytes in cancer: a systematic review with meta-analysis. Br J Cancer 2011;105:93–103.
8. Tavare R, McCracken MN, Zettlitz KA, Knowles SM, Salazar FB, Olafsen T, et al. Engineered antibody fragments for immuno-PET imaging of endogenous CD8+ T cells in vivo. Proc Natl Acad Sci U S A 2014;111:1108–13.

9. Tavare R, Escuin-Ordinas H, Mok S, McCracken MN, Zettlitz KA, Salazar FB, et al. An effective immuno-PET imaging method to monitor CD8-dependent responses to immunotherapy. Cancer Res 2016;76:73–82.
10. Pandit-Taskar N, Postow MA, Hellmann MD, Harding JJ, Barker CA, O'Donoghue JA, et al. First-in-humans imaging with (89)Zr-Df-IAB22M2C anti-CD8 minibody in patients with solid malignancies: preliminary pharmacokinetics, biodistribution, and lesion targeting. J Nucl Med 2020;61:512–9.
11. Sharma SK, Lyashchenko SK, Park HA, Pillarsetty N, Roux Y, Wu J, et al. A rapid bead-based radioligand binding assay for the determination of target-binding fraction and quality control of radiopharmaceuticals. Nucl Med Biol 2019;71:32–8.
12. Cheng DT, Mitchell TN, Zehir A, Shah RH, Benayed R, Syed A, et al. Memorial Sloan Kettering-Integrated Mutation Profiling of Actionable Cancer Targets (MSK-IMPACT): a hybridization capture-based next-generation sequencing clinical assay for solid tumor molecular oncology. J Mol Diagn 2015;17:251–64.
13. Chaney AM, Johnson EM, Cropper HC, James ML. PET imaging of neuroinflammation using [11C]DPA-713 in a mouse model of ischemic stroke. J Vis Exp 2018;136:57243.
14. Walsh NC, Kenney LL, Jangalwe S, Aryee KE, Greiner DL, Brehm MA, et al. Humanized mouse models of clinical disease. Annu Rev Pathol 2017;12:187–215.
15. De La Rochere P, Guil-Luna S, Decaudin D, Azar G, Sidhu SS, Piaggio E. Humanized mice for the study of immuno-oncology. Trends Immunol 2018;39:748–63.
16. Brehm MA, Shultz LD, Luban J, Greiner DL. Overcoming current limitations in humanized mouse research. J Infect Dis 2013;208:S125–30.
17. Knowles SM, Wu AM. Advances in immuno-positron emission tomography: antibodies for molecular imaging in oncology. J Clin Oncol 2012;30:3884–92.
18. Tawbi HA, Forsyth PA, Algazi A, Hamid O, Hodi FS, Moschos SJ, et al. Combined nivolumab and ipilimumab in melanoma metastatic to the brain. N Engl J Med 2018;379:722–30.
19. Goldberg SB, Schalper KA, Gettinger SN, Mahajan A, Herbst RS, Chiang AC, et al. Pembrolizumab for management of patients with NSCLC and brain metastases: long-term results and biomarker analysis from a non-randomised, open-label, phase 2 trial. Lancet Oncol 2020;21:655–63.
20. Brown CE, Alizadeh D, Starr R, Weng L, Wagner JR, Naranjo A, et al. Regression of glioblastoma after chimeric antigen receptor T-cell therapy. N Engl J Med 2016;375:2561–9.
21. O'Rourke DM, Nasrallah MP, Desai A, Melenhorst JJ, Mansfield K, Morrissette JJD, et al. A single dose of peripherally infused EGFRvIII-directed CAR T cells mediates antigen loss and induces adaptive resistance in patients with recurrent glioblastoma. Sci Transl Med 2017;9:eaaa0984.
22. Cloughesy TF, Mochizuki AY, Orpilla JR, Hugo W, Lee AH, Davidson TB, et al. Neoadjuvant anti-PD-1 immunotherapy promotes a survival benefit with intratumoral and systemic immune responses in recurrent glioblastoma. Nat Med 2019;25:477–86.
23. Schalper KA, Rodriguez-Ruiz ME, Diez-Valle R, Lopez-Janeiro A, Porciuncula A, Idoate MA, et al. Neoadjuvant nivolumab modifies the tumor immune microenvironment in resectable glioblastoma. Nat Med 2019;25:470–6.
24. Keskin DB, Anandappa AJ, Sun J, Tirosh I, Mathewson ND, Li S, et al. Neoantigen vaccine generates intratumoral T cell responses in phase Ib glioblastoma trial. Nature 2019;565:234–9.
25. Chen DS, Mellman I. Oncology meets immunology: the cancer-immunity cycle. Immunity 2013;39:1–10.
26. Galldiks N, Lohmann P, Albert NL, Tonn JC, Langen K-J. Current status of PET imaging in neuro-oncology. Neurooncol Adv 2019;1:vdz010.
27. Griessinger CM, Olafsen T, Mascioni A, Jiang ZK, Zamilpa C, Jia F, et al. The PET-tracer 89Zr-Df-IAB22M2C enables monitoring of intratumoral CD8 T cell infiltrates in tumor-bearing humanized mice after T cell bispecific antibody treatment. Cancer Res 2020;80:2903–13.
28. Oh T, Fakurnejad S, Sayegh ET, Clark AJ, Ivan ME, Sun MZ, et al. Immunocompetent murine models for the study of glioblastoma immunotherapy. J Transl Med 2014;12:107.
29. Ashizawa T, Iizuka A, Nonomura C, Kondou R, Maeda C, Miyata H, et al. Antitumor effect of programmed death-1 (PD-1) blockade in humanized the NOG-MHC double knockout mouse. Clin Cancer Res 2017;23:149–58.